Multitechnique characterization of oligo(ethylene glycol) functionalized gold nanoparticles

Ali Rafati[a)]
National ESCA and Surface Analysis Center for Biomedical Problems, Departments of Chemical Engineering and Bioengineering, University of Washington, Box 351653, Seattle, Washington 98195-1653

Alexander G. Shard
National Physical Laboratory, Teddington, Middlesex TW11 0LW, United Kingdom

David G. Castner[b)]
National ESCA and Surface Analysis Center for Biomedical Problems, Departments of Chemical Engineering and Bioengineering, University of Washington, Box 351653, Seattle, Washington 98195-1653

(Received 31 August 2016; accepted 25 October 2016; published 9 November 2016)

Gold nanoparticles (AuNPs) with average diameters of ~14 and ~40 nm, as well as flat gold coated silicon wafers, were functionalized with oligo ethylene glycol (OEG) terminated 1-undecanethiol $(HS\text{-}CH_2)_{11}$ self-assembled monolayers (SAMs). Both hydroxyl $[(OEG)_4OH]$ and methoxy $[(OEG)_4OMe]$ terminated SAMs were prepared. The AuNPs were characterized with transmission electron microscopy (TEM), time of flight secondary ion mass spectrometry (ToF-SIMS), x-ray photoelectron spectroscopy (XPS), attenuated total reflectance Fourier infrared spectroscopy (ATR-FTIR), and low-energy ion scattering (LEIS). These studies provided quantitative information about the OEG functionalized AuNPs. TEM showed the 14 nm AuNPs were more spherical and had a narrower size distribution than the 40 nm AuNPs. ToF-SIMS clearly differentiated between the two OEG SAMs based on the $C_3H_7O^+$ peak attributed to the methoxy group in the OMe terminated SAMs as well as the different masses of the $[Au + M]^-$ ion (M = mass of the thiol molecule) from each type of SAM. Overlayer/substrate ratios quantitatively determined with XPS show a greater proportion of OEG units at the surface of 40 nm AuNPs compared to the 14 nm AuNPs. ATR-FTIR suggested the C11 backbone of the two SAMs on both AuNPs are similar and crystalline, but the OEG head groups are more crystalline on the 40 nm AuNPs compared to the 14 nm AuNPs. This indicated a better ordered SAM present at the surface of the larger, more irregular particles due to greater ordering of the OEG groups. This was consistent with the XPS and LEIS results, which showed a 30% thicker SAM was formed on the 40 nm AuNPs compared to the 14 nm AuNPs. The OH or OMe functionality did not have a significant effect on the ordering and thickness of the OEG SAMs. © *2016 American Vacuum Society*. [http://dx.doi.org/10.1116/1.4967216]

I. INTRODUCTION

In recent years, there has been a significant interest in colloidal gold nanoparticles (AuNPs) for applications such as personal care products and drug delivery,[1–3] as well as materials with readily customizable size, shape,[4] and chemistry.[5] The extensive surface analysis of such materials with nanometer dimensions is therefore crucial to understand how their synthesis and subsequent functionalization affects the final properties.[6,7] This information is important for optimizing the function of engineered nanoparticles in research and commercial uses,[5,8–16] but unfortunately in many studies it is often neglected. Recently, model systems have been produced to develop methodologies for characterization of functionalized colloidal nanomaterials;[8,15,17–23] however, it is necessary to further increase the range of model self-assembled monolayer (SAM) chemistries that are well characterized and increase the complexity of the functionalization process since many of the AuNPs being developed for biomedical applications are first covered with a mixed thiol SAM where the individual thiols can contain multiple species (e.g., alkyl chain + ethyl glycol chain + reactive terminal group) followed by covalent attachment of biomolecules (peptides, proteins, DNA, etc.).

Oligo ethylene glycol (OEG) and poly(ethylene glycol) (PEG) functionalized surfaces are desirable for biomedical applications due to their ability to reduce protein adsorption,[24,25] which can otherwise lead to activation of an immune response and renal clearance. PEGylated AuNPs have been investigated to ascertain their therapeutic usefulness.[26,27] In this work, a model system of OEG functionalized AuNPs is characterized in detail using multiple, complementary techniques to provide an improved understanding of these funtionalized AuNPs. Future studies will characterize the covalent attachment of proteins to the OEG functionalized AuNPs.

[a)]Present address: 3M Company, 3M Center, 201-S-264-A, St. Paul, MN 55144.
[b)]Electronic mail: castner@uw.edu

II. EXPERIMENTAL METHODS

A. Materials

Hydrogen tetrachloroaurate(III) trihydrate (99.9% $HAuCl_4 \cdot 3H_2O$) and sodium citrate dihydrate (trisodium salt, $C_6H_5Na_3O_7 \cdot 2H_2O$) were purchased from Sigma-Aldrich. Ethanol (absolute-200 proof) was sourced from Pharmaco-AAPER (Vancouver, WA). Both (1-mercapto-11-undecyl) tetra ethylene glycol and methoxy(ethylene glycol)$_4$ were procured from Assemblon (Seattle, WA). Ultrapure water (resistivity $> 18.0\,M\Omega$/cm) dispensed by a Modulab Analytical research-grade water system (Siemens, Lowell, MA) was used in all sample preparations as well as for the cleaning of glassware. All reagents were used as received and were of analytical grade.

Dialysis tubing (Spectra/Por, regenerated cellulose, molecular weight cut off 50 000) was purchased from VWR Scientific, Inc. Transmission electron microscopy (TEM) grids (Carbon Type-A, 300 mesh, copper grids) were purchased from Ted Pella, Inc. (Redding, CA). Silicon wafers were purchased from Silicon Valley Microelectronics and diced into $1 \times 1\,cm^2$ pieces and then cleaned with a series of organic solvent washes. Flat Au substrates were produced by depositing a 10 nm film of Ti followed by 100 nm of Au (99.9%) using a CHA 600 Electron Beam Evaporator at pressures below 1×10^{-6} Torr.

B. AuNP preparation

AuNPs were synthesized using a modified Turkevich method described elsewhere.[28,29] Briefly, glassware was cleaned with aqua regia (HCl/HNO_3 in a 3:1 ratio) to remove any previous gold contamination and rinsed with copious amounts of ultrapure water to remove any residual acid. A 0.01% (w/v) $HAuCl_4$ aqueous solution was heated to 100 °C and maintained at this temperature for the entire synthesis in a reflux system under nitrogen. A 1% aqueous solution of $C_6H_5Na_3O_7$ was added in volumetric ratios of 2.5:100 and 1:100 to make AuNPs with average diameters of 14 and 40 nm, respectively. The synthesis was allowed to continue for 30 min, and then cooled to room temperature before being stored at 4 °C until required for analysis.

C. AuNP functionalization

Stock solutions of 1 mM of each thiol were produced by dissolving them in ethanol. A 2× excess of concentration of 100 μM of each thiol was added to 100 ml of AuNPs and stirred for 2 min before sonicating for 1 min, and then, the AuNPs were left to functionalize for 2 days under stirring on a magnetic stir plate. The AuNPs in this study were purified by at least four cycles of centrifugation and redispersal in ultrapure water. An Allegra X-22 centrifuge (Beckman Coulter, Pasadena, CA) was used to spin the 14 nm functionalized AuNPs at 8000 rpm for 45 min and the 40 nm functionalized AuNPs at 8000 rpm for 20 min (the larger particles separated faster). The supernatant was extracted and discarded. Purification of the functionalized AuNPs by dialysis was also examined, but not used, as it was observed the proportion of unbound sulfur detected by x-ray photoelectron spectroscopy (XPS) was ~2.8 times higher with the dialysis method compared to the centrifuge and redispersal method, indicating for OEG functionalized AuNPs the centrifuge and redispersal method was more effective than the dialysis method at removing physisorbed thiol molecules. This is in contrast to carboxylic acid terminated SAMs on AuNPs where purification by dialysis was observed to be more effective.[15] The concentrated AuNPs were deposited 10 μl at a time on solvent cleaned silicon wafers and placed under vacuum in a desiccator to dry. The deposition and vacuum desiccation was repeated multiple times to form a sufficiently thick confluent layer of AuNPs for XPS and time of flight secondary ion mass spectrometry (ToF-SIMS) analysis. A complete layer was desirable to avoid any background signal from the underlying silicon substrate. Samples are denoted 14 and 40 followed by the terminal functionality (OH or OMe) in Secs. III and IV to represent SAMs on 14 and 40 nm AuNPs.

D. Au-coated wafer functionalization

A clean Au-coated wafer was immersed in a 100 μM thiol solution in ethanol in a 20 ml glass scintillation vial backfilled with N_2 gas and left for 2 days. The samples were extracted and rinsed with copious amounts of ethanol, then immediately blown dry with a stream of N_2 gas and stored under N_2 until analysis. Samples are denoted by flat followed by the terminal functionality in Sec. III to represent SAMs on flat Au films deposited on silicon wafers.

E. Transmission electron microscopy

A Phillips CM100 transmission electron microscope with a tungsten filament cathode was operated with an emission current of 5–7 μA and a 100 kV accelerating voltage. Images were acquired with a Gatan model 689 digital slow scan camera (Gatan, Inc., Pleasanton, CA). All images were acquired at a 128×128 pixel resolution and used either 130 000 or 180 000 magnification. The images were processed using IMAGEJ (ver. 1.46, NIH, MD) to determine the average size and circularity of the synthesized nanoparticles before functionalization.

F. X-ray photoelectron spectroscopy

A Kratos Axis UltraDLD (Kratos, Manchester, UK) instrument equipped with a monochromatic Al Kα x-ray source was used for XPS analysis. The hybrid mode was used for analysis where photoelectrons, which are relative to the electrostatic mode, collected a wider range of take-off angles, thereby increasing the detected signal for both the quantification and high resolution scans. The survey scans used for quantitation were acquired using an analyzer pass energy of 80 eV, a step size of 1 eV, and dwell time of 200 ms. The C1s, O1s, S2p, and Au4d peak areas were converted into equivalent homogeneous compositions using average matrix relative sensitivity factors.[30] Au4d, rather than Au4f, peaks were chosen because they appear at a

kinetic energy between the C1s and O1s peaks and their use mitigates variabilities associated with XPS instrumental transmission functions and the choice of database for relative sensitivity factors. A recent interlaboratory study of AuNPs coated with peptide SAMS demonstrated that this approach improved the comparability of XPS data between laboratories by a factor of 2.[31] The high-resolution scans were acquired using an analyzer pass energy of 20 eV and a step size of 0.1 eV. The nominal photoelectron take-off angle was 0° (defined as the angle between the substrate normal and the axis of the analyzer lens). Samples were analyzed in duplicate with at least three nonoverlapping measurement areas per sample.

G. Time of flight secondary ion mass spectrometry

A ToF-SIMS V (ION-TOF GmbH, Münster, Germany) was used for ToF-SIMS analysis. Bi_3^+ ions of 25 keV with a current of ~0.07 pA were used for the analysis of $250 \times 250\ \mu m$ regions of the sample with 256×256 pixels. The acquisitions continued until reaching a total primary ion fluence of 5×10^{11} ions/cm^2 per spectrum, which was well below the static limit. Positive and negative secondary ions were collected up to 878 m/z. The positive spectra were mass calibrated using the CH^+, CH_3^+, $C_2H_3^+$, and $C_3H_5^+$ fragments. The negative spectra were mass calibrated using the CH^- OH^-, and C_2H^- fragments. The typical mass resolution was ~5000 at m/z 27 (positive) and m/z 25 (negative). As with XPS, samples were analyzed in duplicate with three nonoverlapping measurement areas per sample.

H. Attenuated total reflectance-Fourier transform infrared spectroscopy

A Bruker Tensor 27 FTIR spectrometer (Bruker, Germany) was used for attenuated total reflectance-Fourier infrared spectroscopy (ATR-FTIR) analysis. A cleaned flat piece of Si coated with vacuum deposited Au measuring 1×1 cm was used as a background standard. Eighty scans were acquired between a range of 4000 and 600 cm^{-1} at a resolution of 8 cm^{-1}.

I. Low energy ion scattering

An ION-TOF Qtac100 (IONTOF GmbH, Münster, Germany) dedicated high sensitivity low-energy ion scattering (HS-LEIS) instrument was used for analysis. The analysis of the samples was performed using 5 nA, 3 keV $^4He^+$ primary ions scanned over a 2×2 mm^2 area. The analysis took 180 s, leading to an ion dose of 1.4×10^{14} ions/cm^2, which is well below the static limit for 3 keV He ions. A flat Au reference sample was analyzed after sputter cleaning with 500 eV Ar^+. For the flat Au reference sample, the sputter beam was scanned over 1.5×1.5 mm^2 while the analysis beam was scanned over 0.75×0.75 mm^2.

III. RESULTS AND DISCUSSION

A. TEM analysis

Representative TEM images for the two sizes of AuNPs synthesized are shown in Fig. 1 along with the corresponding IMAGEJ analysis. A significantly larger sample number for the 14 nm particles was obtained owing to their small size and the low degree of aggregation found on the TEM sample stub (aggregates were excluded from the IMAGEJ analysis).

The size distribution was found to be narrower for the 14 nm AuNPs ($\sigma = 1.0$ nm) than for the 40 nm AuNPs ($\sigma = 6.6$ nm), as shown in Figs. 1(c) and 1(d). Deviations in substrate uniformity is an important consideration for both the formation and characterization of SAMs.[12] Calculating SAM thickness on AuNPs using analytical methods such as simulation of electron spectra for surface analysis [SESSA (Refs. 32 and 33)] or XPS data modeling[18] relies on assumptions made about the uniformity of both size and shape of the SAM functionalized AuNPs. The TEM observed shape of the 40 nm AuNPs suggests they likely contain larger 111 terraces, as such the expectation is that SAM packing could be different on these two different sets of AuNPs.[11,34] Due to the deviation from sphericity for the 40 nm AuNPs (only 35% have a sphericity <1.1) assumptions made when calculating SAM thickness could be more prone to error than for 14 nm AuNPs (82% have a sphericity <1.1). Thus, an additional method, LEIS analysis, has been used in this work to directly determine the average thickness of the SAMs to complement the XPS thickness measurements.[18]

B. ToF-SIMS analysis

Positive and negative ToF-SIMS were used to investigate the AuNPs functionalized with the two SAMs. Key selected regions from these spectra are shown in Figs. 2(a) and 2(b).

Figure 2(a) shows results for the 14 nm samples. Comparable results were observed for the 40 nm and flat samples. Relative intensities were not found to vary considerably between the functionalized 14 nm AuNPs, 40 nm AuNPs, and flat films. In Fig. 2(a), the OH and OMe terminated SAMs are readily distinguished from one another by the relative intensities of the $C_2H_5O^+$ and $C_3H_7O^+$ secondary ions. The $C_2H_5O^+$ ion can be formed from ethylene glycol units in the OEG chains of both OH and OMe OEG SAMs and from the terminal ethylene glycol unit on the OH OEG SAM. The $C_3H_7O^+$ ion predominately is formed from the terminal ethylene glycol unit on the OMe OEG SAM. The spectra demonstrate significantly higher intensity for the $C_2H_5O^+$ ion from the OH OEG SAM sample compared to the OMe OEG SAM sample. For the OMe OEG SAM sample, a comparable excess intensity is found for the $C_3H_7O^+$ ion. It is reasonable to conclude that the excess intensity in both cases derives from the end-group and this is consistent with previous studies of end-group contribution to SIMS spectra for bulk OEG samples.[35] Since both of these low mass fragments are present in the spectra of both OEG

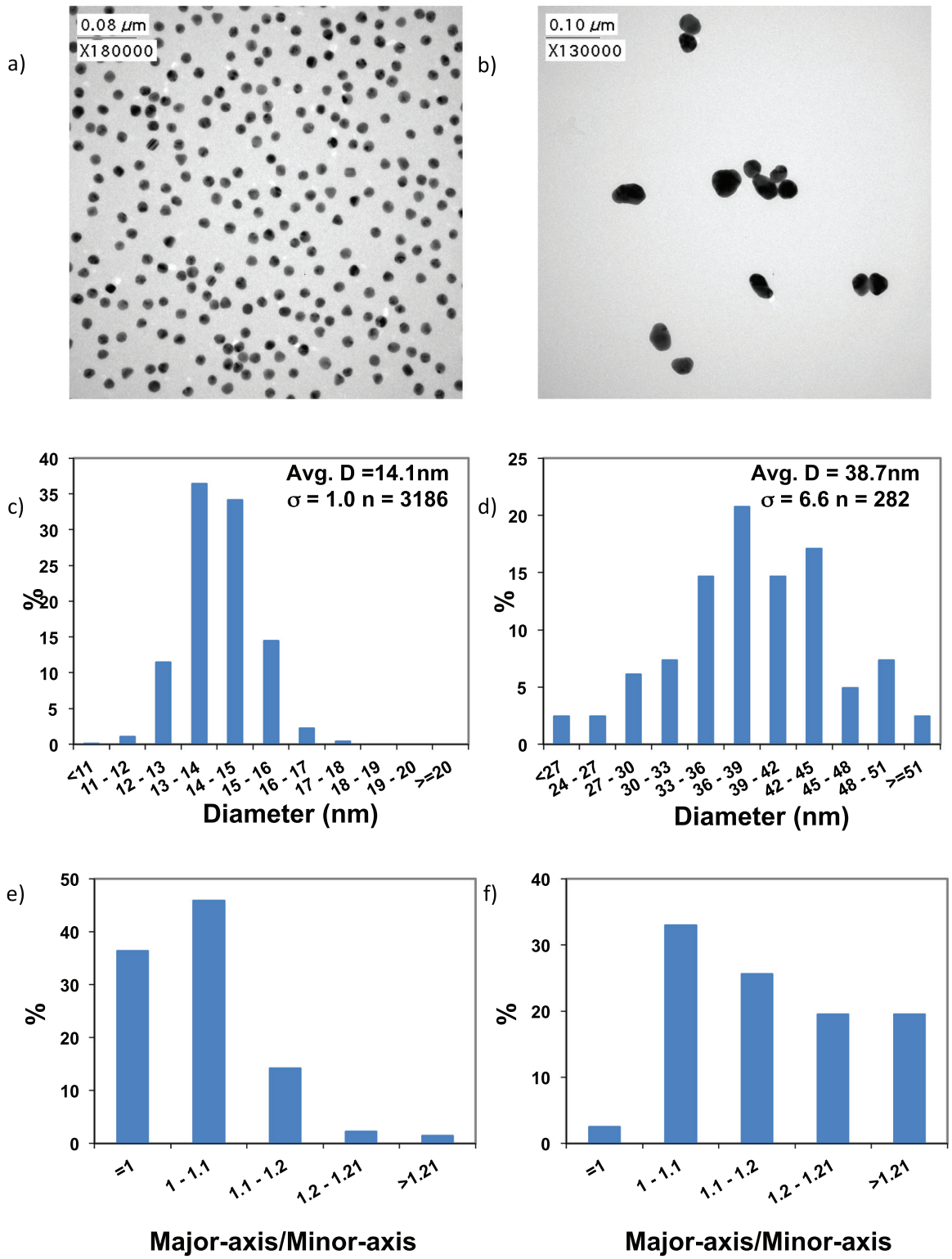

FIG. 1. TEM and particle analysis showing representative images of (a) 14 nm and (b) 40 nm AuNPs with corresponding IMAGEJ determined size distributions for (c) 14 nm and (d) 40 nm AuNPs and the sphericity (the ratio between the major and minor axis of each particle determined with IMAGEJ) for (e) 14 nm and (f) 40 nm AuNPs. Thresholding in the IMAGEJ analysis was used to exclude particles that were clearly agglomerations of 2 or more nanoparticles.

SAMs, the high mass regions shown in Fig. 2(b) were examined to further confirm and identify the presence of the two different terminal groups.

The left hand panel of Fig. 2(b) shows the high mass range of the negative secondary ion spectra where the $[Au + M]^-$ ion (M = mass of thiol molecule) at m/z 591.24 u from the OMe terminated thiol is located. As expected, only the OMe SAMs on the 14 and 40 nm AuNPs exhibited peaks at m/z 591.24 u. The right hand panel of Fig. 2(b) shows the high mass range of the negative secondary ion spectra where

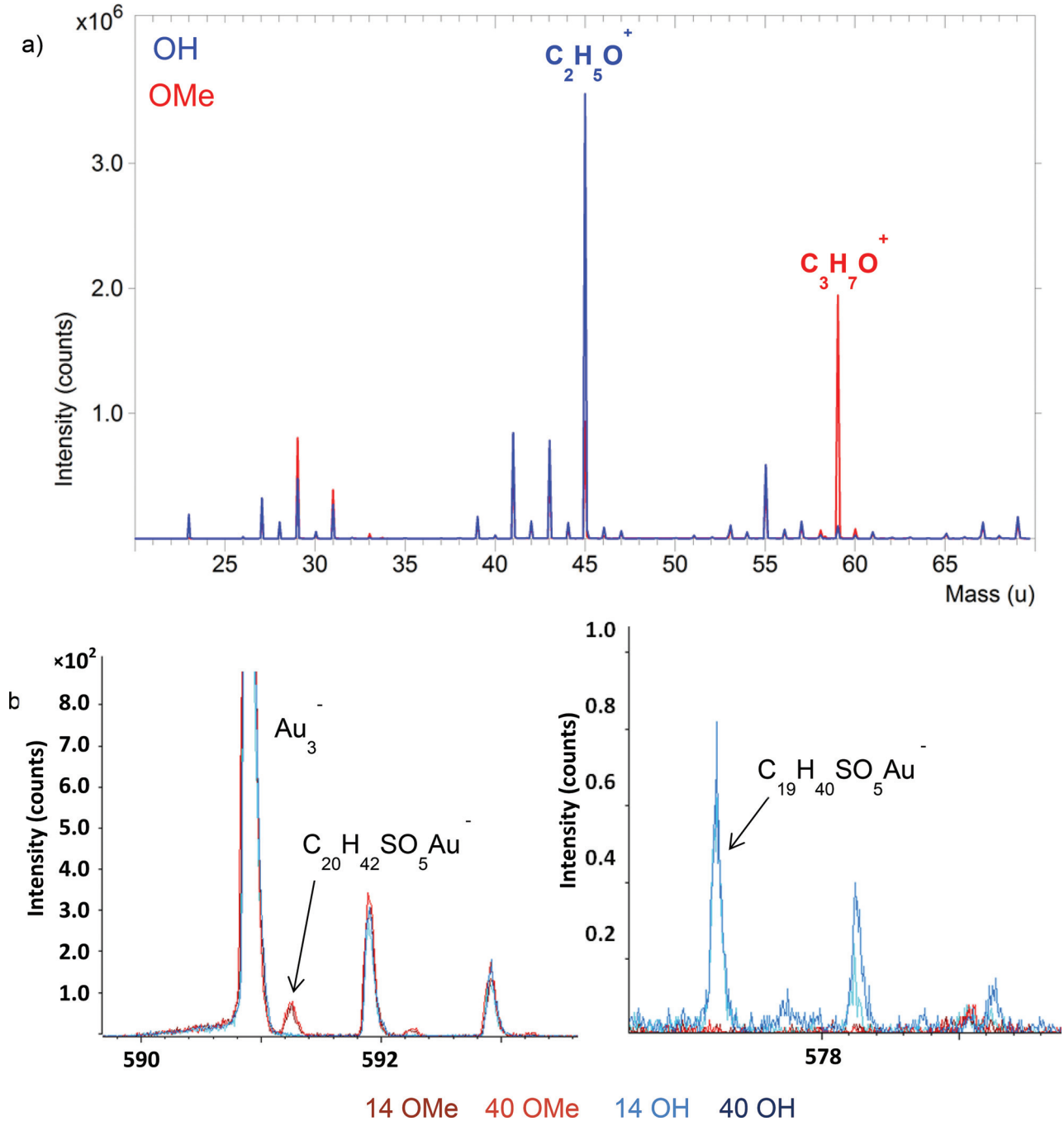

FIG. 2. (a) Overlay of the positive ToF-SIMS data from the 14 OH and 14 OMe samples over a mass range of 20–70 m/z u. (b) High mass region around the $[Au + M]^-$ ion in the negative ion spectra with the four spectra (14 OMe, 14 OH, 40 OMe, and 40 OH) overlaid. Each type of SAM (OMe and OH) produced similar spectra on both the 14 and 40 nm AuNPs; so, similar shades of red were used for the OMe spectra, and similar shades of blue were used for the OH spectra.

the [Au + M] ion at m/z 577.23 u from the OH terminated thiol is located. As expected, only the OH SAMs on the 14 and 40 nm AuNPs exhibited peaks at m/z 577.23 u. The spectra in Fig. 2(b) show the expected functionalization of the AuNPs was achieved as the correct [Au + M] signals were observed from the OH and OMe SAMs. In addition, ratios of isotopic peaks associated with the [Au + M] fragment are consistent with expectations for both SAMs. Although ToF-SIMS can readily differentiate the OEG SAMs with different terminal groups, the size of the AuNPs did not have a significant effect on the normalized [Au + M] secondary ion intensity.

C. XPS analysis

XPS detected C, O, and S from the SAM overlayers and Au from the underlying substrates. No other elements were detected. Surface compositions were determined for all samples using standard procedures that assume heterogeneous depth distribution of all elements (see Table I). Since these

TABLE I. Equivalent elemental compositions in atomic percentage determined from XPS analysis of the OH and OMe SAMs on 14 nm, 40 nm and flat gold substrates along with the C/O ratios calculated from those values. The number in parentheses for the atomic percentage indicates the standard deviation from six measurements.

Substrate	Element (at. %)	OH SAM	OMe SAM
14 nm AuNPs	C	59.6 (0.7)	59.5 (0.8)
	O	17.8 (0.8)	17.9 (0.7)
	S	1.8 (0.2)	1.6 (0.0)
	Au	20.8 (0.3)	21.0 (0.4)
	C/O ratio	3.35	3.32
40 nm AuNPs	C	60.0 (1.3)	59.9 (0.8)
	O	19.2 (0.8)	19.5 (0.8)
	S	1.4 (0.2)	1.2 (0.1)
	Au	19.4 (0.6)	19.5 (0.5)
	C/O ratio	3.12	3.07
Flat gold	C	50.1 (0.7)	47.8 (1.5)
	O	15.1 (0.4)	13.3 (0.4)
	S	1.3 (0.3)	1.6 (0.2)
	Au	33.5 (0.8)	37.3 (0.9)
	C/O ratio	3.32	3.59

materials consist of an organic coating on gold, the equivalent gold composition reflects the thickness of the organic coating as well as the size and shape of the NPs.

Table I shows the XPS determined surface elemental compositions for all samples prepared in this study. The significant difference in the measured compositions between the two AuNP samples and the flat Au sample is due to the high surface curvature of AuNPs and the ~10 nm sampling depth of XPS. The full range of photoelectron take-off angles is detected from the AuNP samples, but not for the flat Au samples. Thus, the C and O intensities from the OEG SAMs are increased, and the Au intensities from the NP cores are decreased due to the increased contributions that the off-normal photoelectron take-off angles make to overall measured XPS compositions for the SAM covered AuNPs. The similar XPS equivalent compositions of the two AuNP samples is in contrast to previous studies of SAMs on AuNPs where with decreasing particle size the signals from the SAM overlayer increase relative to the signal from the AuNP core.[36] This indicates the structure or density of the OEG SAMs is different on the 14 and 40 nm AuNPs. The Au and S concentrations are slightly lower on the 40 nm AuNPs compared to the 14 nm AuNPs. Previous studies have observed decreased Au concentrations for the same SAM with the same thickness as the AuNP size decreases.[15] Therefore, if the SAM overlayer were of the same thickness, the equivalent Au concentration for the 14 nm particles should be lower than that of the 40 nm particles. Here, the opposite is observed and this suggests the OEG SAMs form a thicker or more densely packed SAM on the 40 nm AuNPs compared to the 14 nm AuNPs which would result in more attenuation of the Au and S intensities and a consequent increase in carbon and oxygen intensities.

The higher O concentration on the 40 nm AuNPs compared to the 14 nm AuNPs suggests that more EG subunits may be present at the outermost surface of the OEG SAMs on the 40 nm AuNPs. These differences could be due to different ordering of the OEG SAMs on the 14 and 40 nm AuNPs. The AuNPs particles are synthesized and functionalized in an aqueous environment, with different particle size distributions and shapes observed for the 14 nm vs 40 nm AuNPs, which could influence the packing and order of the SAMs formed on the AuNPs. The hydrophobic effects previously observed for OMe SAMs compared to OH SAMs have been proposed to affect the SAM packing density on flat gold surfaces by influencing the chain flexibility.[24]

The equivalent concentration of gold found in this analysis can be directly converted into an organic overlayer thickness using a direct method described previously[18] and extended for the specific case of organic coatings on gold particles.[37] The method relies upon the assumption of sphericity in the particle and shell, a central core, knowledge of the effective attenuation lengths of electrons, and the intensity of XPS signals from pure materials. The effect of non-ideal particle morphology on XPS data has been studied,[23] and significant errors can arise if the coating is not uniform and a spherical model with a central core is employed. The effect of shape for the OEG/AuNPs is expected to be quite minor, i.e., less than the relative error in attenuation lengths (~10%), provided the majority of particles are close to spherical or have random orientations on the surface. The results of these calculations for the OEG/AuNPs are shown in Table II in comparison to the LEIS analysis.

The stoichiometric ratio of carbon to oxygen for the compounds OEG OH and OEG OMe are 3.8 and 4, respectively. Within the ethylene glycol moiety, the ratio is close to 2. Neglecting the possibility of hydrocarbon contamination and topographical effects, we would expect the experimental ratios to lie between these values, and that the value will be lower if the SAM is more ordered, since the oxygen bearing ethylene glycol part will be closer to the surface. Table I shows that the 14 OH and 14 OMe samples have a ratio closer to that of a disordered system (C/O = 3.3), but the 40 OH and 40 OMe samples appear to be more ordered (C/O = 3.1). For the AuNP samples, the direct comparison is valid. The fact that the flat samples have C/O ratios in Table I (3.32 and 3.59 for OH and OMe, respectively) similar or slightly higher than that of the 14 nm samples should not be taken as an indication that these surfaces are more disordered, because topographic effects are important here. For a flat, well ordered sample, this ratio is a function of photoelectron

TABLE II. Average thickness of the OEG SAMs for each type of substrate analyzed with HS-LEIS and XPS. For comparison, the thickness calculated based on average bond lengths and accounting for a 30° tilt of the chain axis from the surface normal is 2.7 nm.

Substrate	Average SAM thickness, LEIS (nm)	Average SAM thickness, XPS (nm)
14 nm AuNPs	2.0 ± 0.1	1.4 ± 0.1
40 nm AuNPs	2.6 ± 0.1	1.8 ± 0.1
Flat gold	1.9 ± 0.1	1.7 ± 0.1

take-off angle, and the ratio would be expected to decrease as grazing incidence is approached. Model calculations using a straight-line approximation for a well-ordered film indicate that the ratio should be approximately 3.32 and 3.57 for OH and OMe, respectively, at an emission angle normal to the surface and 2.95 and 3.22, respectively, at an emission angle 60° from normal, which is an approximate "average angle" for a particle. This analysis suggests that the OEG SAMS on a flat surface have a structure more similar to those on the 40 nm particles than on the 14 nm particles.

Results from the XPS high-resolution spectra shown Fig. 3 provide further information about the OEG SAM overlayer. Representative C1s and S2p spectra are shown with their corresponding peak fits in Figs. 3(a) and 3(b). The S2p spectra of all OEG SAMs were similar on all substrates. The dominant sulfur species was the thiolate (S2p3/2 BE of 162 eV).[38] A small amount of unbound thiol (S2p3/2 BE of 163.5 eV) was observed on all samples.[38]

Two carbon species, ether and hydrocarbon, were present in the C1s spectra, as expected from the structure of the OEG thiols. The ether to hydrocarbon intensity ratios determined from the high resolution C1s peak fits are shown in Fig. 3(c). The type of SAM terminal group did not have a significant effect on this ratio for the two AuNP samples. However, this ratio did vary among the different substrates the OEG SAMs were deposited onto. The ether to hydrocarbon ratio was observed to increase as flat Au < 14 nm AuNPs < 40 nm

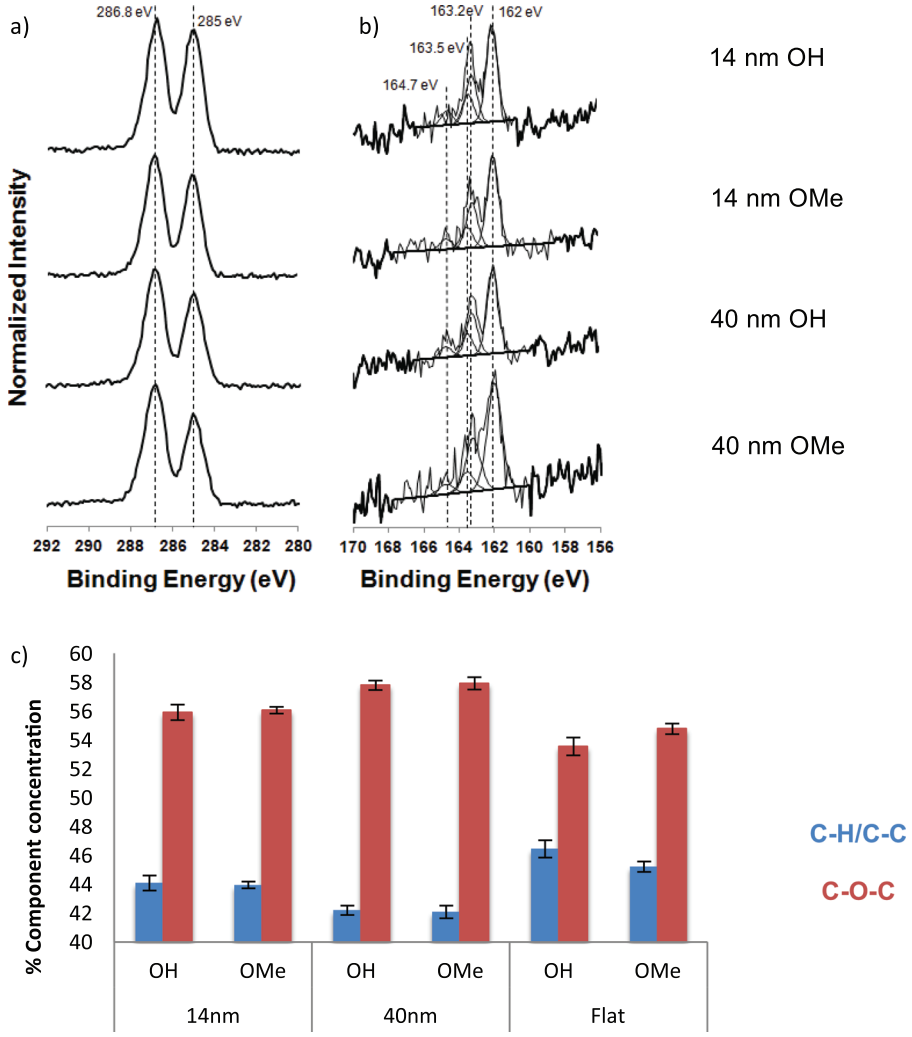

Ratio	14 OH	14 OMe	40 OH	40 OMe	Flat OH	Flat OMe
Ether/ C-C	1.27 (0.03)	1.28 (0.01)	1.37 (0.02)	1.38 (0.03)	1.15 (0.01)	1.21 (0.02)

FIG. 3. XPS (a) C1s and (b) S2p high-resolution spectra for OEG SAMs on AuNPs and flat Au surfaces. The S2p components were fit as previously described (Ref. 38). (c) Comparison of the amounts of ether and hydrocarbon species determined from the C1s spectra of the OEG SAMs on AuNP and flat Au surfaces.

AuNPs. This is consistent with the trend observed in the carbon to oxygen ratios. The stoichiometric ether/HC ratio is 0.9 for the OEG OH thiol molecule and 1.0 for the OEG OMe thiol molecule. The XPS measured ether/HC ratios for all samples are greater than 1.1, indicating the OEG units are enriched at the outermost surface of the OEG SAMs for all samples. We note that hydrocarbon contamination on the surface of these materials will act to reduce this ratio and so these results are a conclusive demonstration of the orientation of the OEG molecules. A larger ether/HC ratio indicates a greater degree of order in the SAM, although topographic effects are important here also, and direct comparison can only be made between the 40 and 14 nm particles. As 40 nm AuNPs show the highest ether/HC ratio this indicates that the OEG SAMs formed on larger, more irregular in shape AuNPs have a greater OEG surface enrichment than the OEG SAMs formed on the smaller more spherical NPs. For a well-ordered SAM on a flat surface, the ratio should be approximately 1.2 at an emission angle normal to the surface rising to 1.7 at an emission angle 60° from normal.

D. ATR-FTIR analysis

The extent of SAM ordering on the 14 and 40 nm AuNPs was investigated with ATR-FTIR as shown in Fig. 4, which contains the methylene stretch and the ether stretch regions for the OH and OMe SAMs.

The ordering of the alkane portion of the OEG thiol molecules were determined by monitoring the position of the CH_2 stretching frequencies [see Fig. 4(a)]. Well-ordered alkane SAMs in the literature show CH_2 asymmetric stretches below 2920 cm^{-1} ($\nu CH_{2,asym}$).[39,40] As we consistently observed values that were less than those values, we conclude that the C11 alkane SAM backbone is generally well ordered and have comparable ordering regardless of AuNP size, topography, and OEG terminal group.

The ether stretch (C-O-C) from the EG subunits presented in Fig. 4(b) shows a significant shift between the SAMs present on two sizes of AuNPs. A small difference is observed between the two SAMs on the 14 nm AuNPs, with the peak from the 14 OH SAM appears at a few wavenumbers lower than the peak from the 14 OMe SAM. The ether stretches from both OEG SAMs on the 40 nm AuNPs were significantly lower (1097 cm^{-1}) than on the 14 nm AuNPs (1108–1114 cm^{-1}). Based on the results from previous studies, the ether stretches observed on the OEG SAMs on 40 nm AuNPs indicate that those samples contain more ordered or crystalline OEG units compared to OEG SAMs on 14 nm AuNPs.[41] The more disordered nature of the OEG units on the 14 nm AuNPs is consistent with a thinner, less densely packed SAM on the 14 nm AuNPs. This may be due to smaller areas of 111 terraces and a higher density of edge and corner atoms on the 14 nm AuNPs. The significance of increased OEG crystallinity is that crystalline OEG chains have been shown to adsorb significant amounts of protein while disordered OEG chains have been shown to resist protein adsorption.[24] As such, the OEG SAMs on 14 and 40 nm AuNPs would be expected to exhibit a significant difference when placed in the biological environment.

E. LEIS analysis

In LEIS, a beam of low energy noble gas ions are directed at a sample and the scattering of those incident ions and the subsequent energy loss of the detected scattered ions can be directly related to the elemental composition of the surface. Recent advances in HS-LEIS instrumentation allows for greater sensitivity to the analysis of different atomic layers (i.e., "depth profiling") and a reduction in damage, particularly to organic material.[42,43] HS-LEIS is now capable of giving static (nondestructive) depth profiles over the outermost 5–10 nm.[43–46] Thus, HS-LEIS was used here to characterize the thickness of the OEG SAM overlayers on AuNPs. Previously, beam induced damage would accumulate over the course of the LEIS analysis degrading organic films and providing inaccurate results; however, now with advances in instrumentation, HS-LEIS can provide accurate measurements of the overlayer thickness.

A description of how such analysis is undertaken is described elsewhere.[47] Briefly, the background intensity is caused by ions that have penetrated the SAM overlayer and scattered from Au core of the NPs. These scattered ions lose energy when passing through the SAM layer. This loss of

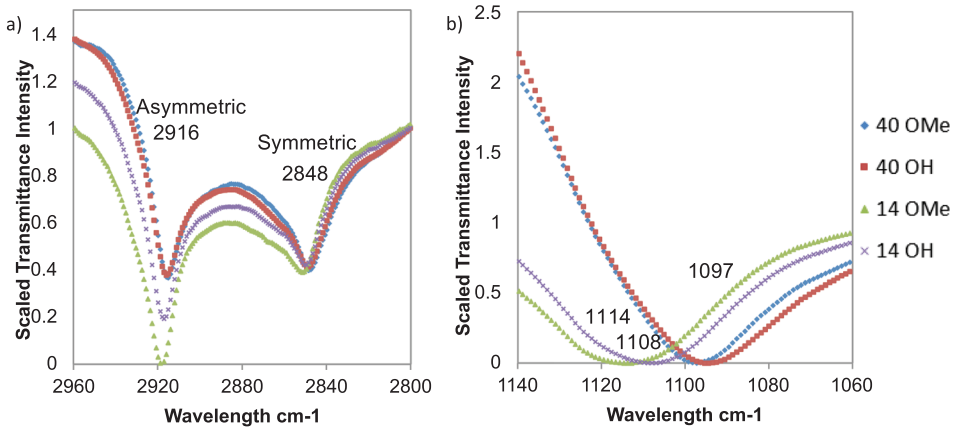

FIG. 4. ATR-FTIR spectra for the OEG SAMs on AuNPs in (a) the CH_2 stretch region and (b) the ether stretch region.

energy can be related to the overlayer thicknesses. It has been previously shown for SAMs on Au surfaces that the relationship between the background peak on the SAM covered samples and the peak observed for a clean, flat Au surface is estimated to be 90 eV/nm for alkenethiol SAMs.[44] Thus, using this relationship, the thickness of the SAM can be precisely determined when the scattering background is fitted with an error function and the energy loss of its inflection point from the clean surface peak measured (see Fig. 5).

Figure 5 shows the energy loss spectra of the $^4He^+$ ions detected from the OEG SAM covered AuNPs compared to a flat, ion beam etched 100 nm Au coated Si wafer reference. The difference between the loss peak from the SAM covered AuNPs and the clean Au reference shows the SAM thickness on 14 nm AuNPs is significantly thinner than the SAM thickness on 40 nm AuNPs. Terminal functionalization (OH vs OMe) did not have a detectable on the measured thicknesses, as expected based on prior analysis.[24]

The experimentally derived values are tabulated in Table II and compared with calculations from the averaged XPS data.[18] The thickness from a line drawing based on stoichiometry, using typical bond lengths and angles as well as applying a 30° tilt of the chain axis from the surface normal [typical value reported for alkanethiol SAMs (Refs. 12 and 48)], was calculated to be 2.7 nm. Significantly thicker SAMs (30%) were found on the 40 nm AuNPs compared with 14 nm AuNPs, both by HS-LEIS and XPS. The discrepancy in the values obtained by the two methods is discussed later. Considering the ATR-FTIR results discussed above, the SAM thickness measurements are consistent with the presence of a more well-packed, crystalline OEG SAM on the surface of the 40 nm AuNPs.

For the flat gold sample, XPS and LEIS provide thickness values that are consistent. This is a reasonable validation of the methods used for data interpretation, which are well

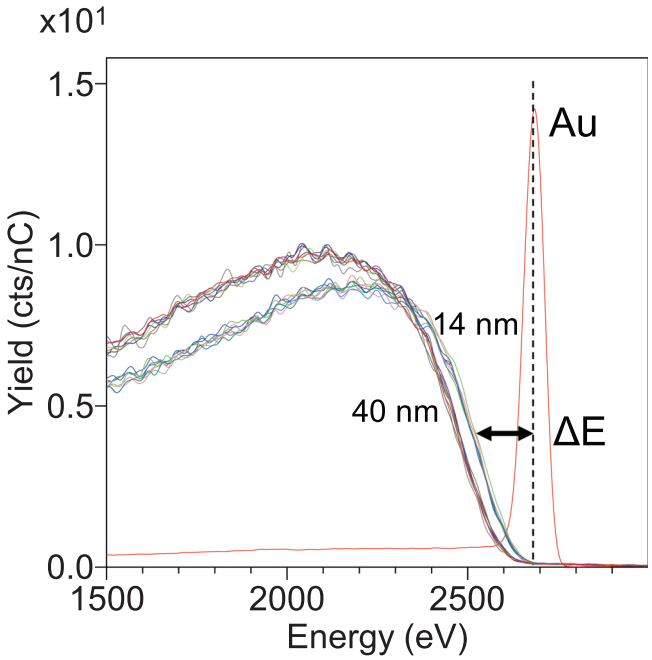

FIG. 5. HS-LEIS SAM results for OEG SAMs on 14 and 40 nm AuNPs.

described for flat surfaces. The accuracy of the value for LEIS depends upon the assumption of the energy loss of 90 eV/nm obtained for alkenethiol SAMs.[44] Currently, there is no assessment of the general validity of this energy loss. In the original paper,[44] the value is expressed as 8 eV per carbon atom in the SAM, and the value has been converted under some assumptions about the thickness of the layers that were originally used. It is also worth noting that 1.5 keV $^4He^+$ primary ions were used in that work compared with 3 keV $^4He^+$ primary ions used here. For XPS, the accuracy is largely dependent upon the estimates used for the intensities of the pure materials, the method chosen for background subtraction and the electron effective attenuation lengths. In this case, a relative accuracy of better than 20% can be estimated.

For the nanoparticles, the thickness calculated by XPS relies upon the same fundamental data as that used for the flat sample, but accounts for the topography using a method that has been validated through simulation. Both the results from the thickness measurements, and also considerations of the effect of geometry on the elemental composition and C1s shape provided above, indicate that the OEG SAMs on the 40 nm samples are similar to those on the flat surfaces. Therefore, it is interesting that the direct LEIS results for the 40 nm particles are rather different from the flat surface. Here, we note that no correction for topography is included in the analysis of LEIS results. For a flat surface with a defined scattering angle, all ions scattered from gold experience the same path length through the organic overlayer. On a particle there are a large range of path lengths depending upon the impact parameter of the primary ion and the azimuthal scattering angle. Some path lengths are shorter and some longer and the distribution of these depends upon the relative core radius and coating thickness. Due to neutralization effects, describing the effect of this on a LEIS spectrum is not a trivial matter. A recent versailles project on advanced materials and standards study on measuring the organic overlayer thickness on gold particles included LEIS data, where some participants applied a topographic correction factor of 0.74.[31] It is interesting to note that, if we assume that the OEG SAM on the flat surfaces and the 40 nm particles are identical, a correction factor of 0.73 is implied. Then, the LEIS result for the 14 nm particles is corrected with a factor of 0.73, and this results in an OEG SAM thickness of 1.5 nm, which is consistent with the XPS result.

Following this reasoning, our results indicate that the packing density of OEG SAMs on the 14 nm particles is lower than that on 40 nm particles, which have a similar packing density to flat surfaces. For flat surfaces, this density translates to between 3 and 3.5 molecules per nm^2, which is lower than alkanethiol packing densities, which are typically in the region of 5 molecules per nm^2.[49,50]

IV. CONCLUSIONS

This study uses a multitechnique, complementary approach to characterizing Au surfaces functionalized with OEG SAMs. The results from TEM, XPS, ToF-SIMS, ATR-

FTIR, and HS-LEIS showed the OEG SAMs were more well-ordered and thicker on the 40 nm AuNPs compared to the 14 nm AuNPs. The 40 nm AuNPs had a broader size distribution and were more nonspherical compared to 14 nm AuNPs. Thus, it is likely the 40 nm AuNPs had larger low index terrace regions [e.g., (111) terraces] and a lower percent of edge and corner atoms, which could be responsible for the more well-ordered OEG SAMs formed on the 40 nm AuNPs. While these differences between the two sizes of AuNPs had a significant effect on the structure of the OEG SAMs, no effect of the OEG terminal functionality (OH vs OMe) on SAM structure or thickness was detected. The ordering and thickness of the two OEG SAMs on each surface were the same, within the experimental error. Determining the role that AuNP shape and OEG terminal group play in functionalized AuNPs is essential for understanding their structure–function relationships as well as their for potential *in vivo* applications. These results reinforce the importance of fully characterizing each functionalized AuNP formulation and highlights how differences between substrates can have a significant effect on the assembly of thiols onto the AuNPs. It shows that the structure and thickness of a SAM formed on one particle size and shape of AuNPs can be significantly different on other particle sizes and shapes of AuNPs. Comparison of XPS and LEIS data indicates that a topographic correction factor for thickness measurements obtained from LEIS is required, and, for these samples, the factor is near 0.73.

ACKNOWLEDGMENTS

The financial support for this work was provided by Grant No. EB-002027 from the National Institutes of Health to NESAC/BIO. The authors thank Thomas Grehl and IONTOF (GmbH) for the use of their HS-LEIS instrumentation and expertise to measure the thickness of the OEG SAM overlayers. The authors thank Yung-Chen Wang for discussions and assistance with the XPS analysis of the OEG SAM overlayers. Part of this work was conducted at the Molecular Analysis Facility, a National Nanotechnology Coordinated Infrastructure site at the University of Washington that is supported in part by the National Science Foundation (Grant No. ECC-1542101), the University of Washington, the Molecular Engineering and Sciences Institute, and the Clean Energy Institute.

[1]D. Pissuwan, T. Niidome, and M. B. Cortie, J. Controlled Release **149**, 65 (2011).
[2]S. D. Brown *et al.*, J. Am. Chem. Soc. **132**, 4678 (2010).
[3]J. Nam, N. Won, H. Jin, H. Chung, and S. Kim, J. Am. Chem. Soc. **131**, 13639 (2009).
[4]Y. G. Sun and Y. N. Xia, Science **298**, 2176 (2002).
[5]M.-C. Daniel and D. Astruc, Chem. Rev. **104**, 293 (2004).
[6]D. R. Baer *et al.*, J. Vac. Sci. Technol., A **31**, 50820 (2013).
[7]L. E. Marbella and J. E. Millstone, Chem. Mater. **27**, 2721 (2015).
[8]D. R. Baer, D. J. Gaspar, P. Nachimuthu, S. D. Techane, and D. G. Castner, Anal. Bioanal. Chem. **396**, 983 (2010).
[9]D. R. Baer *et al.*, Surf. Interface Anal. **40**, 529 (2008).
[10]A. Frydman, D. G. Castner, M. Schmal, and C. T. Campbell, J. Catal. **157**, 133 (1995).
[11]D. W. Grainger and D. G. Castner, Adv. Mater. **20**, 867 (2008).
[12]J. C. Love, L. A. Estroff, J. K. Kriebel, R. G. Nuzzo, and G. M. Whitesides, Chem. Rev. **105**, 1103 (2005).
[13]C. J. Powell, A. Jablonski, W. S. M. Werner, and W. Smekal, Appl. Surf. Sci. **239**, 470 (2005).
[14]S. D. Techane, L. J. Gamble, and D. G. Castner Biointerphases **6**, 98 (2011).
[15]S. D. Techane, L. J. Gamble, and D. G. Castner J. Phys. Chem. C **115**, 9432 (2011).
[16]G. K. Wertheim and S. B. DiCenzo Phys. Rev. B **37**, 844 (1988).
[17]M. Chudzicki, W. S. M. Werner, A. G. Shard, Y.-C. Wang, D. G. Castner, and C. J. Powell, J. Phys. Chem. C **119**, 17687 (2015).
[18]A. G. Shard, J. Phys. Chem. C **116**, 16806 (2012).
[19]W. S. M. Werner, M. Chudzicki, W. Smekal, and C. J. Powell, Appl. Phys. Lett. **104**, 243106 (2014).
[20]M. D. Torelli, R. A. Putans, Y. Tan, S. E. Lohse, C. J. Murphy, and R. J. Hamers, ACS Appl. Mater. Interfaces **7**, 1720 (2015).
[21]G. Zorn, S. R. Dave, X. Gao, and D. G. Castner, Anal. Chem. **83**, 866 (2011).
[22]D. J. H. Cant, Y.-C. Wang, D. G. Castner, and A. G. Shard, Surf. Interface Anal. **48**, 274 (2016).
[23]Y.-C. Wang, M. H. Engelhard, D. R. Baer, and D. G. Castner, Anal. Chem. **88**, 3917 (2016).
[24]L. Y. Li, S. F. Chen, J. Zheng, B. D. Ratner, and S. Y. Jiang, J. Phys. Chem. B **109**, 2934 (2005).
[25]P. Kingshott, S. L. McArthur, H. Thissen, D. G. Castner, and H. J. Griesser, Biomaterials **23**, 4775 (2002).
[26]D. Shenoy, W. Fu, J. Li, C. Crasto, G. Jones, C. DiMarzio, S. Sridhar, and M. Amiji, Int. J. Nanomed. **1**, 51 (2006).
[27]H. Otsuka, Y. Nagasaki, and K. Kataoka, Adv. Drug Delivery Rev. **55**, 403 (2003).
[28]G. Frens, Nature **241**, 20 (1973).
[29]J. Turkevich, P. C. Stevenson, and J. Hillier, Discuss. Faraday Soc. **11**, 55 (1951).
[30]M. P. Seah, I. S. Gilmore, and S. J. Spencer, J. Electron Spectrosc. Relat. Phenom. **120**, 93 (2001).
[31]N. A. Belsey *et al.*, J. Phys. Chem. C **120**, 24070 (2016).
[32]S. Techane, D. R. Baer, and D. G. Castner, Anal. Chem. **83**, 6704 (2011).
[33]W. Smekal, W. S. M. Werner, and C. J. Powell, Surf. Interface Anal. **37**, 1059 (2005).
[34]A. C. Templeton, W. P. Wuelfing, and R. W. Murray, Acc. Chem. Res. **33**, 27 (2000).
[35]A. G. Shard, M. C. Davies, and E. Schacht, Surf. Interface Anal. **24**, 787 (1996).
[36]W. D. Luedtke and U. Landman, J. Phys. Chem. **100**, 13323 (1996).
[37]N. A. Belsey, A. G. Shard, and C. Minelli, Biointerphases **10**, 019012 (2015).
[38]D. G. Castner, K. Hinds, and D. W. Grainger, Langmuir **12**, 5083 (1996).
[39]M. D. Porter, T. B. Bright, D. L. Allara, and C. E. D. Chidsey, J. Am. Chem. Soc. **109**, 3559 (1987).
[40]M. M. Walczak, C. Chung, S. M. Stole, C. A. Widrig, and M. D. Porter, J. Am. Chem. Soc. **113**, 2370 (1991).
[41]P. Harder, M. Grunze, R. Dahint, G. M. Whitesides, and P. E. Laibinis, J. Phys. Chem. B **102**, 426 (1998).
[42]H. R. J. ter Veen, T. Kim, I. E. Wachs, and H. H. Brongersma, Catal. Today **140**, 197 (2009).
[43]H. H. Brongersma, M. Draxler, M. de Ridder, and P. Bauer, Surf. Sci. Rep. **62**, 63 (2007).
[44]H. H. Brongersma, T. Grehl, P. A. van Hal, N. C. W. Kuijpers, S. G. J. Mathijssen, E. R. Schofield, R. A. P. Smith, and H. R. J. ter Veen, Vacuum **84**, 1005 (2010).
[45]R. L. Puurunen *et al.*, J. Appl. Phys. **96**, 4878 (2004).
[46]G. C. Vanleerdam, K. M. H. Lenssen, and H. H. Brongersma, Nucl. Instrum. Methods Phys. Res., Sect. B **45**, 390 (1990).
[47]A. Rafati, H. R. J. ter Veen, and D. G. Castner, Surf. Interface Anal. **45**, 1737 (2013).
[48]L. Strong and G. M. Whitesides, Langmuir **4**, 546 (1988).
[49]T. Laredo, J. Leitch, M. Chen, I. J. Burgess, J. R. Dutcher, and J. Lipkowski, Langmuir **23**, 6205 (2007).
[50]G. E. Poirier, E. D. Pylant, and J. M. White, J. Chem. Phys. **104**, 7325 (1996).